

Tailored Broad-Spectrum Emission in Hybrid Aggregation Induced Emission (AIE)-MOFs: Boosting White Light Efficiency in Electrospun Janus Microfibers

Vishal Kachwal, Samraj Mollick, and Jin-Chong Tan*

Advances in energy-efficient lighting and display technologies demand innovative materials with tailored broad-spectrum emission properties. Hybrid aggregation-induced emission metal-organic frameworks (AIE-MOFs) offer a promising avenue, combining unique characteristics of organic and inorganic components to yield enhanced luminescence efficiency and robust material stability. The study introduces a spectrum of D (donor)-A (acceptor) type AIE-active ligands into MOFs, enabling tunable emission across the visible spectrum, thus underscoring the versatility of these hybridized MOF materials. The emission properties of AIE-MOFs are further harnessed by integrating them into polymer matrices, resulting in high-performance electrospun fibers with tunable emission. A significant achievement involves the fabrication of Janus-type white light-emitting AIE-MOF fiber composites via side-by-side electrospinning, accomplishing a high quantum yield of 58%, which doubled the performance of homogeneous fibers. Complementing the experimental findings, micro-Raman and nano-Fourier transform infrared spectroscopy are employed as local spectroscopic probes, affording a deeper understanding of the material properties and the mechanisms contributing to enhance light emission. In the understanding, this study presents an unconventional implementation of hybrid AIE-MOFs in Janus-type structures for white light emission. It significantly improves the efficiency of white light sources in optoelectronics, charting a promising direction for future research in the emergent AIE-MOF field.

bandwidth of devices ranging from lighting and displays, to sensors and bio-imaging technology.^[1,2] The road to perfecting these emission properties is paved with a diverse set of approaches, each of which is tuned to cater to the idiosyncrasies of specific material systems and desired emission characteristics.^[3]

The unique strengths and constraints of organic and inorganic materials make them potential players in the quest for optimal emission properties.^[4,5] However, in the realm of hybrid composite materials, specifically metal-organic frameworks (MOFs), we witness a harmonious melding of the advantages of both organic and inorganic components. This fusion promises stability and broad-spectrum emission that traditional materials might not be able to deliver consistently.^[6,7]


In the bustling world of material science, conventional MOFs have long held the spotlight, their unique properties inspiring countless research endeavors. However, beneath their shimmering facade lies an Achilles heel – their emission efficiency is often undermined by the non-radiative decay pathways.^[8] Scientists have ventured down two promising avenues in

response to this challenge. The first involves confinement of luminescent guests (LGs) within MOFs, an approach known as LG@MOFs.^[4,9] Despite its potential; this strategy presents a number of obstacles, such as structural stability issues, control over guest incorporation, long-term efficiency, and leaching.^[4] The second approach, like a beacon of hope, offers possible solutions to these challenges. This path led to the creation of a novel class of MOFs, the aggregation-induced emission active MOFs (AIE-MOFs).^[10,11] These MOFs are designed to leverage rotation-restricted emission, a fresh perspective on improving luminescence efficiency.^[11,12] A groundbreaking study by Dong et al.^[13] demonstrated pioneering work of tunable luminescent AIE-MOFs. Their work crafted a new direction for controlling the local environment and interactions between AIE-active molecules and the MOF framework, resulting in amplified AIE effects and enhanced luminescence efficiency.^[14] This pioneering research has illuminated a promising pathway for developing efficient, tunable, luminescent MOF-based materials.^[15,16] Yet,

1. Introduction

Tuning of emission properties sits at the heart of many photonic applications, underpinning the color, intensity, and spectral

V. Kachwal, S. Mollick, J.-C. Tan
Multifunctional Materials & Composites (MMC) Laboratory
Department of Engineering Science
University of Oxford
Parks Road, Oxford OX1 3PJ, UK
E-mail: jin-chong.tan@eng.ox.ac.uk

 The ORCID identification number(s) for the author(s) of this article can be found under <https://doi.org/10.1002/adfm.202308062>

© 2023 The Authors. Advanced Functional Materials published by Wiley-VCH GmbH. This is an open access article under the terms of the Creative Commons Attribution License, which permits use, distribution and reproduction in any medium, provided the original work is properly cited.

DOI: 10.1002/adfm.202308062

even as recent studies advance the field with host-guest hybrid MOFs for white light emission, challenges persist.^[17] The quest for better intrinsic parameters such as quantum yield (QY) and leaching control remains an ongoing journey.^[18] The exploration continues, with researchers like Yang et al.^[19] pushing the boundaries by creating single-phase white light emissive materials using an encapsulation method, although hurdles like leaching and precise control of the concentration within the single-phase MOF still persisted.^[20]

Stepping away from MOFs, electrospun fibers have also made their mark, with their high surface area to volume ratio, high porosity, and diverse morphologies allowing for future integration into electronic devices.^[21] These attributes have carved out a niche for electrospun fibers in applications spanning from sensing, drug delivery, and energy, to optoelectronics.^[22] Further, AIE-active electrospun fibers present exciting new opportunities in a wide range of technological sectors.^[23]

In the landscape of photonic technologies, we find a marriage of innovation and utility in integrating AIE-active materials with electrospun fibers. This alliance has triggered a sea of change, enhancing photostability,^[24] photothermal & photodynamic properties,^[25] quantum yield,^[26] sensing,^[27] and device sensitivity. The methodology surpasses the constraints of traditional systems such as phosphor-converted (light emitting diodes) LEDs, multi-chip systems, (organic-LEDs) OLEDs, and (quantum dot-LEDs) QLEDs.^[28] At the heart of this innovation is the restriction of intramolecular rotation in AIE compounds and the vast surface area of electrospun fibers, a combination that enables tunable and amplified quantum yield.^[23,29]

Our exploration leads us to Janus fibers, a specific type of electrospun fibers fabricated by side-by-side electrospinning, opening yet another door for innovation.^[30] These composite materials are not just versatile but also unique in their structure. Janus fibers are characterized by their asymmetric structure, often having two distinct sides with different chemical physical properties. Their bifunctionality or multifunctionality extends their applicability across a broad range of fields.^[31] For example, they can be engineered for controlled drug release in medical applications, offer asymmetric photothermal properties for all-weather smart textiles, and are promising in environmental applications like sustainable oil-water separation.^[32] Building on this unique structure, Janus fibers are lauded for their ability to incorporate different materials and functionalities within a single micro- or nanoscale architecture.^[33] The result is a material that can be tailored to specific applications, from textiles,^[34] white light emission^[35] and sensors to drug delivery systems,^[36] tissue engineering,^[37] and antimicrobial materials.^[33] The fusion of AIE-MOFs with these electrospun fibers could herald a new era of composite materials, surpassing the performance of traditional polymer films, composite materials and mixed-matrix membranes. These exciting prospects could illuminate the path forward in the pursuit of tailoring emission properties and creating novel photonic technologies. However, this strategy remains largely explored in the MOF domain.

In this study, we meticulously designed and synthesized hybridized AIE-MOFs through a strategic post-synthetic modification process (Figure 1a), using propeller-shaped AIE ligands to manipulate the emission properties. The chemical structure of hybridized AIE-MOFs is given in Figure 1b. The resulting emis-

sion spectrum of the hybridized AIE-MOFs is fine-tuned to span the entire visible light range. These hybridized AIE-MOFs were integrated with standard electrospun fibers using polyurethane (PU) polymers to enhance the quantum yield. The outcome was a fiber emission with an expertly tailored spectral output within the visible range, yielding a higher quantum yield than the original AIE-MOF powders.

The hybrid AIE-MOFs and fiber's structure, morphology, and optical and electronic properties were systematically evaluated. A comprehensive set of complimentary techniques was employed, including X-ray diffraction (XRD), near-field infrared nanospectroscopy (nano-FTIR), micro-Raman spectroscopy, scanning electron microscopy (SEM), X-ray photoelectron spectroscopy (XPS), photoluminescence (PL) spectroscopy, and UV-vis diffused reflectance spectroscopy (DRS).

Further, we fabricated Janus-type structural white light emissive composites comprising flexible fibers, using the side-by-side electrospinning method (Figure 1c). These fibers exhibited a high quantum yield (QY) of 58%. This is among the highest reported QY for white light-emitting materials based on single-phase hybridized AIE-MOF fibers. Our work underlines the potential of AIE-MOF-based white light-emitting fibers with tailored emission profiles, signposting the route towards developing highly efficient white light sources suitable for a broad spectrum of practical applications.

2. Results and Discussion

In this study, Our exploration has been particularly directed towards three distinguished MOFs, namely NH₂-UiO-66 (Zr) (UiO: University of Oslo), NH₂-MIL-53 (Al), and NH₂-MIL-68 (In) (MIL: Material Institute Lavoisier), owing to their high pore volumes and robustness conducive for post-synthetic modifications under mild acidic and basic conditions, rendering them suitable candidates for applications requiring endurance and stability under varying conditions. The unique structural and chemical characteristics of these MOFs are imperative for our study. NH₂-UiO-66 (Zr) showcases a robust and porous architecture anchored by zirconium metal clusters, with particle sizes ranging between 100 to 200 nm and an ortho-octahedral structural configuration accompanied by pore sizes of 0.8 and 1.1 nm.^[38,39] Conversely, NH₂-MIL-53 (Al) incorporates aluminum metal clusters and is known for its flexible "breathing" behavior, presenting 1D diamond-shaped pores that adapt dynamically to external stimuli, with pore sizes of 0.8 and 1.3 nm.^[40] Conversely, NH₂-MIL-68 (In) embodies indium metal clusters and deviates in its structural framework by featuring a 2D hexagonal channel-like architecture with three distinct types of pore windows of varying geometries, having average openings of 0.5 nm (cubic), 0.7 nm (trigonal), and 2.0 nm (hexagonal).^[41] Each of these MOFs, with their distinct structural and chemical traits, cater to different realms of applications, thus highlighting their potential versatility in gas storage, separation, and other relevant domains.

2.1. Synthesis and Characterization of MOF Powders

The synthesis procedure for MOFs is detailed in the Supporting Information (SI) and follows the published procedures for NH₂-

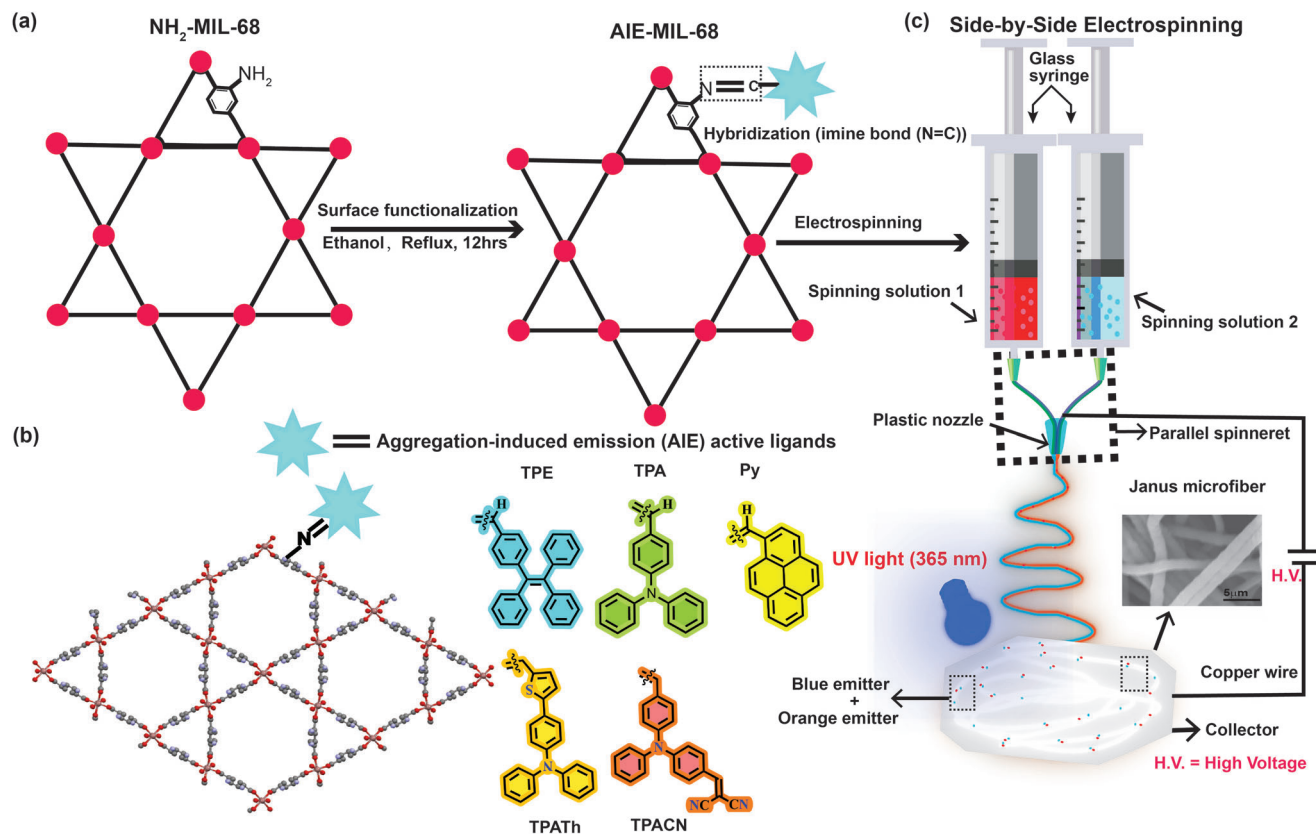


Figure 1. Schematic illustration of the process: a) Strategy for synthesizing hybridized AIE-MOFs. b) Chemical structure representation of different AIE-MOFs (TPE – tetraphenylethylene, TPA – triphenylamine, Py – Pyrene, TPAth-(5-(4-(diphenylamino) phenyl) thiophene-2-carbaldehyde), TPACN – (2-(4-(4-formyl phenyl) (phenyl) amino)benzylidene)malononitrile) c) Side-by-side electrospinning process to fabricate Janus fibers.

UiO-66 (Zr),^[38,39] and NH₂-MIL-53 (Al).^[40] Synthesis of NH₂-MIL-68 (In) was performed utilizing high-concentration reaction method as described in the SI. The covalent approach favors chemically and thermally stable MOFs, which offer a suitable platform for introducing new functional groups.^[42] This allows for incorporating AIE-ligands into the MOF structure through post-synthetic modification (PSM) techniques, an alternative and highly effective synthesis route.

This approach allows for adding appropriate recognition sites into the MOF without changing their topologies while restricting pre-functionalization synthesis. Here we started synthesizing TPA-MIL-68 by covalently linking TPA-CHO with free NH₂ groups in NH₂-MIL-68 (In) at 70 °C in ethanol under nitrogen atmosphere for 12 hours (detailed reactions are given in the SI under the experimental section). The SEM micrographs of both modified and unmodified MOFs have needle-like shapes indicating a negligible change in the crystal morphology after PSM (Figure S6, Supporting Information). The PXRD patterns of the TPA-MIL-68 shown in Figure 2a were in good agreement with those previously reported and identical to the simulated PXRD patterns,^[43] indicating that the crystalline nature of the parent MOF remained intact in the composites. The Raman shift at 443 cm⁻¹ in TPA-MIL-68, corresponding to the In-O band,^[44] confirms no structural change after hybridization (Figure 2b). The appearance of a peak at 1680 cm⁻¹ (which corresponds to –C = N), as well as the disappearance of peaks around 3082 cm⁻¹

(which corresponds to –NH₂) of NH₂-MIL-68 and 1700 cm⁻¹ (–C = O) of TPACHO in TPA-MIL-68, indicates the formation of an imine bond (Figure 2b). XPS analysis was conducted further to investigate the changes in the chemical environment of NH₂-MIL-68, and the deconvoluted XPS patterns are shown in (Figure 2c,d). After the hybridization of TPA-CHO with NH₂-MIL-68 (In), a new shoulder peak at 399.5 and 399.6 eV appeared in the N1s core level spectra for TPA-MIL-68, corresponding to the imine (–C = N) group and tertiary amine group, respectively. As a complete reaction was difficult to achieve, a broad peak combination of NH/NH₂ with tertiary amine (N) and C-N peak was observed, which also shifted to higher energy by 0.4 eV (from 400.4 to 400.8 eV), likely resulting from the delocalization of electron density from the nitrogen in (NH₂). Figure S7a (Supporting Information) shows two peaks at 445.2 and 452.8 eV, corresponding to the In 3d_{5/2} and In 3d_{3/2} of In (III), respectively. For the O1s XPS spectra of NH₂-MIL-68(In), two peaks can be fitted at 533.5 and 531.8 eV, corresponding to the surface chemisorbed H₂O (or oxygen) and In-O bonding, respectively (Figure S7b, Supporting Information). These two peaks in NH₂-MIL-68(In) were shifted compared with those of TPA-MIL-68 (534.0 and 531.9 eV), indicating the delocalization of electron density over the imine bond (Figure S7c, Supporting Information).^[38,45]

This observation is further supported by the FTIR analysis (Figure S8, Supporting Information), which shows the near disappearance of vibrational bands at 3470 and 3381 cm⁻¹ in

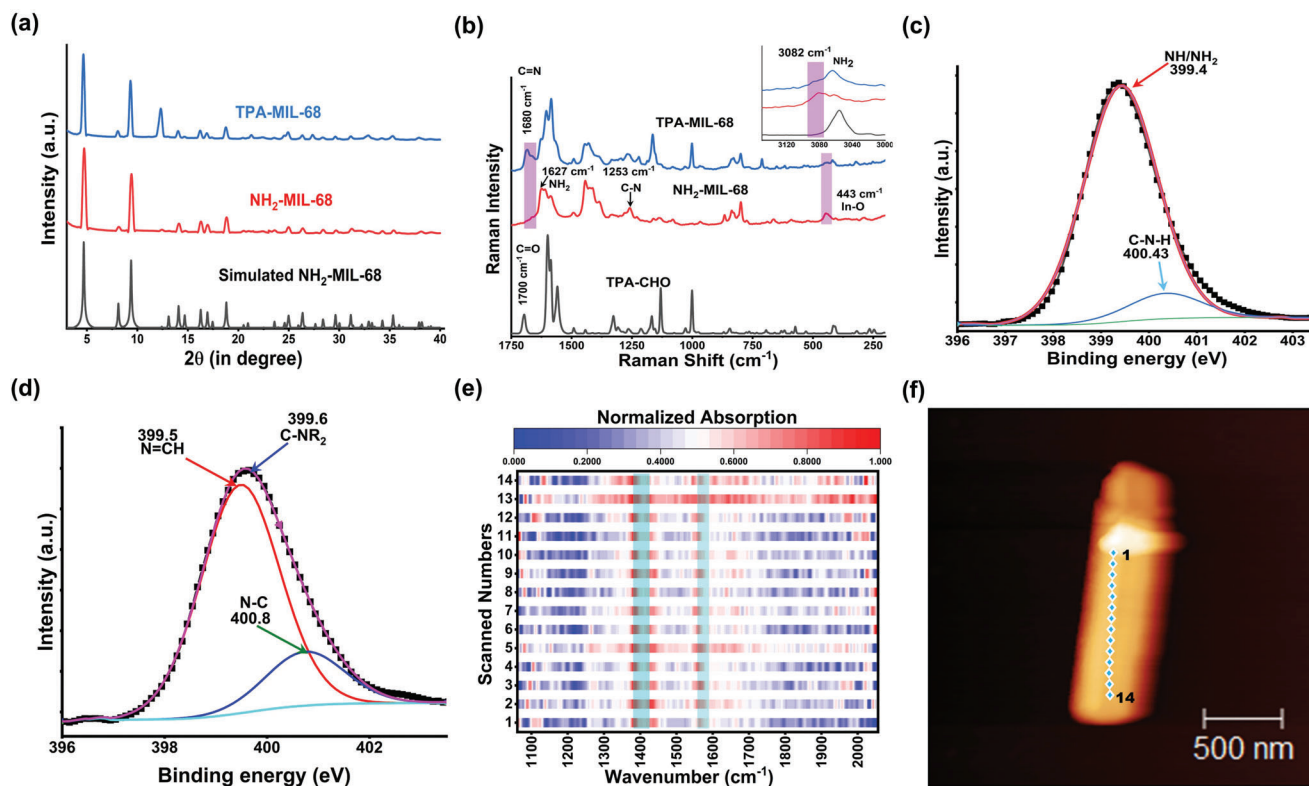


Figure 2. Powder phase characterization of $\text{NH}_2\text{-MIL-68}$ and TPA-MIL-68 . a) PXRD patterns of simulated $\text{NH}_2\text{-MIL-68}$, pristine MOF and hybridized MOF, showing the crystalline nature of the MOF does not change after hybridization with TPA-CHO . b) Raman spectra indicating no major structural changes after hybridization, and confirming the formation of imine bond after reaction. High-resolution XPS patterns of c) N1s of $\text{NH}_2\text{-MIL-68}$ and d) N1s of TPA-MIL-68 . e) Nano FTIR absorption spectra of TPA-MIL-68 crystals taken across the highlighted region in f). The two highlighted bands correspond to the *ca.* $1380\text{--}1390\text{ cm}^{-1}$ (host) and $1580\text{--}1600\text{ cm}^{-1}$ ($\text{C}=\text{N}$) respectively. Fourteen spots on the s-SNOM image f) corresponding to fourteen point-by-point nanoFTIR scans performed locally on the crystal, with a spatial resolution of $\approx 20\text{ nm}$.

TPA-MIL-68 , corresponding to the symmetric and asymmetric stretching of the -N-H group in $\text{NH}_2\text{-MIL-68}$. The band at 1690 cm^{-1} , attributed to the $\text{C}=\text{O}$ group in TPA-CHO , also disappears in TPA-MIL-68 . These results suggest a successful reaction between the $\text{C}=\text{O}$ of the AIE ligand and the NH_2 of the MOF, leading to the formation of an imine bond ($\text{C}=\text{N}$) in TPA-MIL-68 , which appears at $\approx 1581\text{ cm}^{-1}$. Symmetric and asymmetric stretching vibrations of carboxyl bonds are also present in $\text{NH}_2\text{-MIL-68}$. The presence of peaks at 1260 and 773 cm^{-1} , corresponding to the stretching vibrations of C-N and In-O bonds^[45] in TPA-MIL-68 , indicating that the reaction occurs exclusively at the NH_2 group in $\text{NH}_2\text{-MIL-68}$. The near-field nanospectroscopic technique was employed to provide further evidence for the imine bond formation in a single crystal of TPA-MIL-68 .^[46] The obtained nanoFTIR and s-SNOM (Scattering-type scanning near-field optical microscopy) optical image (Figures 2e,f) revealed successful hybridization within the crystals, while retaining the structure of the MOF host indicated by the retention of *ca.* 1380 cm^{-1} band. The nanoFTIR spectra measured at different local spots with 20 nm resolution on the crystals show the ($\text{C}=\text{N}$) imine bond vibrational frequency around $1581\text{--}1600\text{ cm}^{-1}$, confirming the successful formation of imine bonds within the MOF structure. The s-SNOM infrared image of TPA-MIL-68 revealed a long, rectangular block crystal (Figure 2f), consistent with the SEM micrographs of both $\text{NH}_2\text{-MIL-68}$ and TPA-MIL-68 exhibit-

ing a needle-like morphology (Figure S6, Supporting Information). This observation supports the notion that no significant morphological changes occurred during the synthesis process, and the structure of the MOFs is preserved.

2.2. Photophysical Properties of MOF Powders

In order to optimize the amount of AIE-active guest, we conducted a series of reactions between $\text{NH}_2\text{-MIL-68}(\text{In})$ and TPA-CHO , varying the concentration from 0.5 to 2 equivalents (eq) relative to the MOF ligand (2-amino terephthalic acid). We observed slight bathochromic shifts and peak broadening at longer wavelengths in the emission spectra (Figure S9a, Supporting Information). The quantum yield exhibited a minimal decrease beyond using 1 equivalent of TPA-CHO for the reactions (Figure S9b, Supporting Information). The observed broadening of the emission spectra and the slight bathochromic shift might be attributed to the increased concentration of TPA molecules on the MOF surface, causing them to come closer to each other; this, in turn, enhances the $\pi\text{-}\pi$ interaction between the molecules,^[47] resulting in a reduced quantum yield. The FTIR spectra of samples containing 0.5–2 eq of TPA-CHO supported this observation (Figure S10, Supporting Information), as the intensity of the ($\text{C}=\text{N}$) imine peak increased from 0.5 to 1 eq but

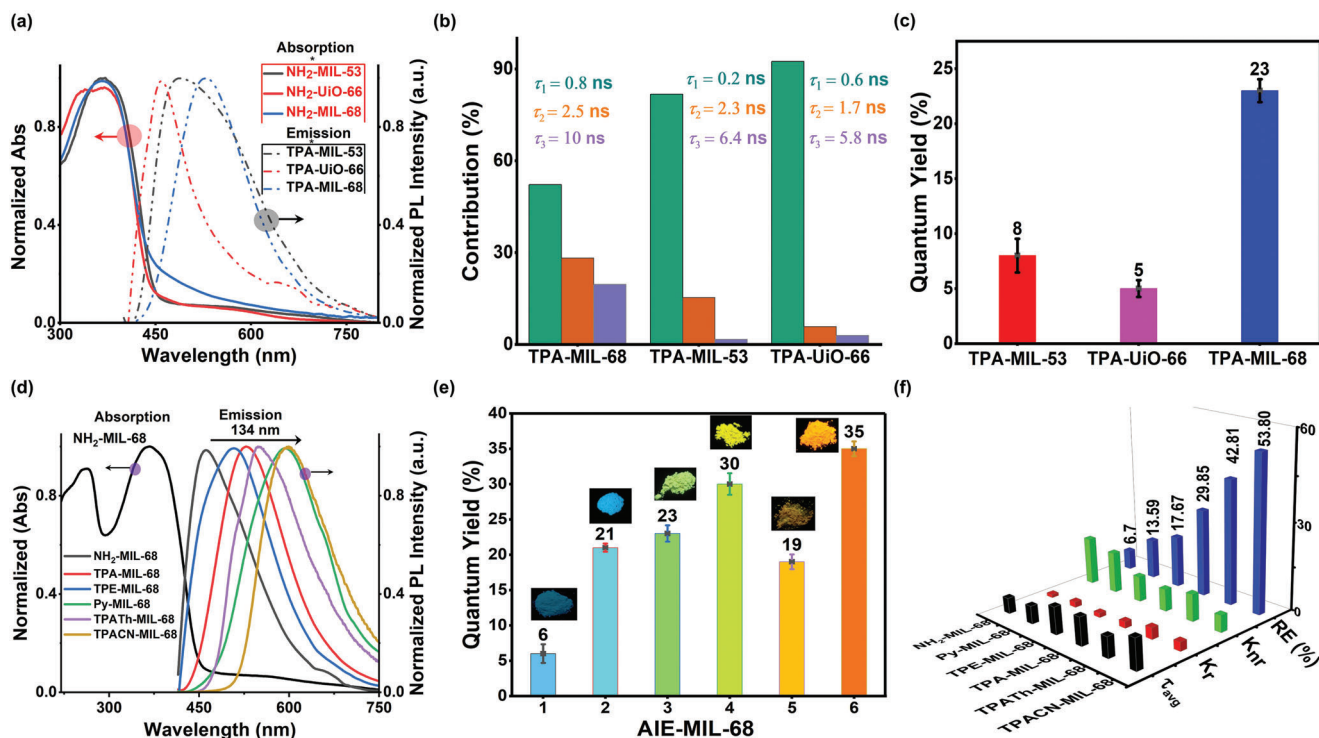


Figure 3. Photophysical characterization of composite powders: a) Normalized UV-vis absorption and photoluminescence spectra. b) Excited state lifetime with components including the relative amplitude (TPA-MIL-68 – λ max = 530 nm, TPA-UiO-66 – λ max = 459 nm, TPA-MIL-53 – λ max = 492 nm). c) Absolute quantum yield for TPA-MIL-68, TPA-MIL-53, and TPA-UiO-66. d) Normalized absorption spectra of NH₂-MIL-68 and photoluminescence spectra of all the hybridized AIE-MIL-68 MOFs. samples denoted as 1) NH₂-MIL-68, 2) TPE-MIL-68, 3) TPA-MIL-68, 4) TPAth-MIL-68, 5) Py-MIL-68, and 6) TPACN-MIL-68 e) Absolute quantum yield (QY) (inset- Photos of AIE-MOF powders subject to a 365-nm UV lamp) and f) Average lifetimes, radiative and non-radiative decay rates of all the hybridized AIE-MOFs calculated by formula $K_r = 1/\tau_0$, $K_{nr} = 1/\tau - K_r$, $\tau_0 = \tau/QY$ and radiative efficiency (RE) % = $(K_r/K_{nr}) \times 100$.

remained almost constant at 2 eq. Moreover, above 1 equivalent, the carbonyl peak increased slightly, indicating the presence of unreacted TPA-CHO adsorbed on the surface of the MOFs, which suggests that a 1:1 stoichiometry in the reaction between the MOF and AIE ligands is optimal. Thus, using one equivalent of TPA-CHO to react with the MOF ligand results in the formation of imine bonds. After optimizing the concentration of the guest ligand in the reaction, we evaluated and compared the emission of TPA-MIL-68 with that of TPA-UiO-66 and TPA-MIL-53. These MOFs were characterized using powder XRD (Figure S11, Supporting Information). The DRS spectral analysis of all modified MOFs reveals prominent absorption bands within the 200–300 nm range, which can be attributed to ligand-to-metal charge transfer (LMCT).^[47,48] Additionally, a well-defined peak in the 350–395 nm range is observed,^[49] suggesting the presence of $n-\pi^*$ transitions^[47] (Figure S12a, Supporting Information). The emissions of TPA-MIL-68, TPA-UiO-66, and TPA-MIL-53 are observed at 530 nm (green emission), 459 nm (blue emission), and 492 nm (light blue emission) (Figure 3a), respectively. In terms of average lifetimes, TPA-MIL-68 exhibits a longer duration (10.04 ns) compared to TPA-MIL-53 (4.58 ns) and TPA-UiO-66 (1.55 ns) (Figure S12b, Supporting Information). Furthermore, the absolute quantum yield of TPA-MIL-68 (QY = 23%) is considerably higher than that of TPA-UiO-66 (5%) and TPA-MIL-53 (8%) (Figure 3c). This disparity in quantum yield un-

derscores the potential influence of factors beyond spectral characteristics, warranting further investigation into the underlying mechanisms employing techniques such as transient absorption spectroscopy.

In the literature, it is evident that the emission intensity of MOFs is influenced not only by the metal ion radius but also by additional factors when the fluorophore concentration remains constant. The metal ion radius is indeed one contributing aspect, and the polarization of the metal ion is another.^[50] Intriguingly, the indium (In) metal ion radius is larger than those of aluminum (Al) and zirconium (Zr) metal ions, yet the quantum yield follows a reverse order. This observation implies that other elements, such as structural disparities, molecular interactions, and varying transition states, may play a significant role in determining the emission intensity of MOFs.^[51]

In the covalently-linked MOFs, an overlap between emission and absorption spectra has been identified (Figure 3a), which may suggest self-quenching effects in these synthesized materials. Lifetime measurements for all MOFs reveal three distinct components (Figure 3b), which may correspond to different relaxation processes, excited-state species, or molecular conformations. The first component (τ_1) may be postulated to be associated with relaxation processes such as vibrational relaxation, internal conversion, or non-radiative decay. Conversely, the second (τ_2) and third (τ_3) components,

characterized by longer lifetimes, could be linked to radiative relaxation processes.^[52,53]

In the comparison of TPA-MIL-68 to TPA-UiO-66 and TPA-MIL-53, the longer components (τ_2 and τ_3) not only have notably shorter lifetimes in the latter two, as shown in Figure 3b, but their contribution is also more significant in TPA-MIL-68 (Figure 3b). This observation could suggest that both LMCT and $n-\pi^*$ transitions in MOFs may be more effectively stabilized; the reasoning was supported by the absorption spectroscopy of the MOFs in which we can observe the slight bathochromic shift (2–5 nm shift) and broadening of the 350 nm peak (Figure S12a, Supporting Information). Introducing the TPA donor molecule through an imine bond could enhance the ligand's electron-donating capacity compared to the bare MOFs, resulting in a more pronounced electron transfer from the lone pair nitrogen to the MOFs through the BDC (benzene dicarboxylic acid) linker. Such increased donating capacity could lead to a more effective stabilization of the excited states associated with the $n-\pi^*$ transitions, possibly contributing to the observed differences in lifetimes and quantum yields among the metal-ion MOFs. In contrast, the high contribution of shorter lifetimes in TPA-UiO-66 and TPA-MIL-53 could indicate faster non-radiative decay processes (Figure 3b), such as excited-state quenching or other deactivation pathways. By the quantum yield measurement and lifetime, we can conclude that the non-radiative decay is less in TPA-MIL-68 compared with the other hybridized MOFs. This could indicate that the excited state transition in TPA-MIL-68 is more effectively stabilized, possibly due to the unique channel type rigid pore structure, which can restrict the TPA molecules, allowing for longer-lived excited states and more efficient radiative decay processes.

Upon observing the higher quantum yield of TPA-MIL-68 compared to other MOFs, we sought to further enhance the optoelectronic properties of NH_2 -MIL-68 by incorporating D-A type AIE-active ligands. We integrated various AIE-active ligands, which include flexible electron donor tetraphenylethylene (TPE) (a well-known AIE active ligand) to rigid electron donor (polyaromatic rings-pyrene), and also triphenylamine (TPA) derivatives synthesized by coupling stronger electron accepting groups like dicyano ($=\text{C}(\text{CN})_2$) and thiophene (Th) to one of the rings. The synthetic procedures and characterization (^1H and ^{13}C NMR spectroscopy) for all AIE ligands can be found in the supporting document (Figures S1–S5, Supporting Information). The PXRD patterns of all the hybridized MOFs agreed with the diffraction patterns of the pristine NH_2 -MIL-68 (Figure S13a, Supporting Information). The presence of the $\text{C}=\text{N}$ (imine bond) $\approx 1581\text{--}1600\text{ cm}^{-1}$ and the disappearance of the NH_2 peak in all the hybridized MOFs (Figure S13b, Supporting Information). The Raman spectra also support the imine bond formation (Figure S13c, Supporting Information). The deconvoluted N1s XPS patterns of TPE-MIL-68 and Py-MIL-68 show a peak at 399.5 eV, while this was observed at 399.6 eV for TPA-MIL-68 and TPACN-MIL-68, corresponding to the imine ($-\text{C}=\text{N}$) group (Figure S13 (d–g), Supporting Information). In TPACN-MIL-68 we can observe a new peak at 401.5 eV corresponding to the CN bond (Figure S13e). TGA shows enhanced thermal stability in MOFs covalently linked with aggregation-induced emission (AIE) ligands (See SI for TGA analysis, Figure S14, Supporting Information). Nitrogen adsorption measurements, con-

ducted at 77 K, were systematically performed on the activated pristine NH_2 -MIL-68(In) and on the TPA derivative modified MOFs (namely TPA-MIL-68, TPA-MIL-68 and TPACN-MIL-68). As depicted in Figure S15 (Supporting Information), all the N_2 sorption isotherms exhibit a Type-I isotherm profile, characteristic of microporous solids. The data revealed a reduction in the uptake of N_2 gas between the pristine and modified MOFs. Furthermore, a comparative scrutiny of the surface areas elucidates the impact of post-synthetic modification on the MOFs. The BET surface area for the pristine NH_2 -MIL-68(In) is $1190\text{ m}^2\text{ g}^{-1}$, while the modified MOFs display diminished values: TPA-MIL-68 at $1005\text{ m}^2\text{ g}^{-1}$, TPACN-MIL-68 at $890.87\text{ m}^2\text{ g}^{-1}$, and TPA-MIL-68 at $810\text{ m}^2\text{ g}^{-1}$. This reduction in surface area and N_2 uptake is ascribed to partial pore blocking induced by post-synthetic modification. We conducted a comprehensive photophysical investigation of hybrid MOFs, revealing intriguing electronic transitions. Excited-state dynamics was analyzed, supplemented by quantum yield measurements and lifetime studies to evaluate excited-state efficiency. Crucially, a new, broad peak at 455 nm emerges in TPACN-MIL-68 and TPA-MIL-68, which may be due to a metal-to-ligand charge transfer (MLCT)^[54] state fostered by a robust electron withdrawing group (Figure S16, Supporting Information).^[55–58] This effective MLCT state leads to an increase in fluorescence efficiency.^[59] A closer examination of the linker's electronic structure through DFT calculations revealed that the HOMO is predominantly distributed across the donor molecule, with a minor portion on the $\text{C}=\text{N}$ group (Figure S17, Supporting Information). The LUMO localizes on the BDC linker upon adding the donor group, shifting towards a more electron-withdrawing moiety when an acceptor is coupled. This denotes an electronic distribution within the hybridized MOFs and indicates a charge density redistribution in the LUMO.

Photoluminescence characteristics reveal distinct emission peaks for the synthesized MOFs, with a considerable bathochromic shift of 134 nm in the emission spectra as the electron-withdrawing groups increase (Figure 3d). The emission color change can be observed by exposing the AIE-MOF powder under UV light (365 nm) (Figure 3e (inset)). This shift underscores the significant influence of these moieties on MOFs' optical properties. The photoluminescent quantum yield increases by an order of magnitude from NH_2 -MIL-68 to TPACN-MIL-68, reflecting higher quantum efficiencies for MOFs with pronounced D–A character (Figure 3e). For further elucidation, parallel experiments were conducted to evaluate the excitation, emission, and quantum yield of the free AIE-CHO ligand, pivotal in the post-synthetic modification. The emission and excitation spectra (Figure S18, Supporting Information) evince a bathochromic shift in emission wavelength from 450 to 595 nm transitioning from TPACHO to TPACN CHO, underscoring the substantial influence of electronic modifications. Comparative analysis of the quantum yield revealed a notable enhancement for the AIE-MOFs relative to the free AIE-CHO ligands (Figure S19, Supporting Information), substantiating the enhancement in photoluminescent properties after post-modification.

Moreover, we have conducted a comprehensive excitation-emission mapping study, as summarized in Figure S20 (Supporting Information). The results accentuated the covalent linkage of the AIE-CHO ligand with the BDC- NH_2 in MOF,

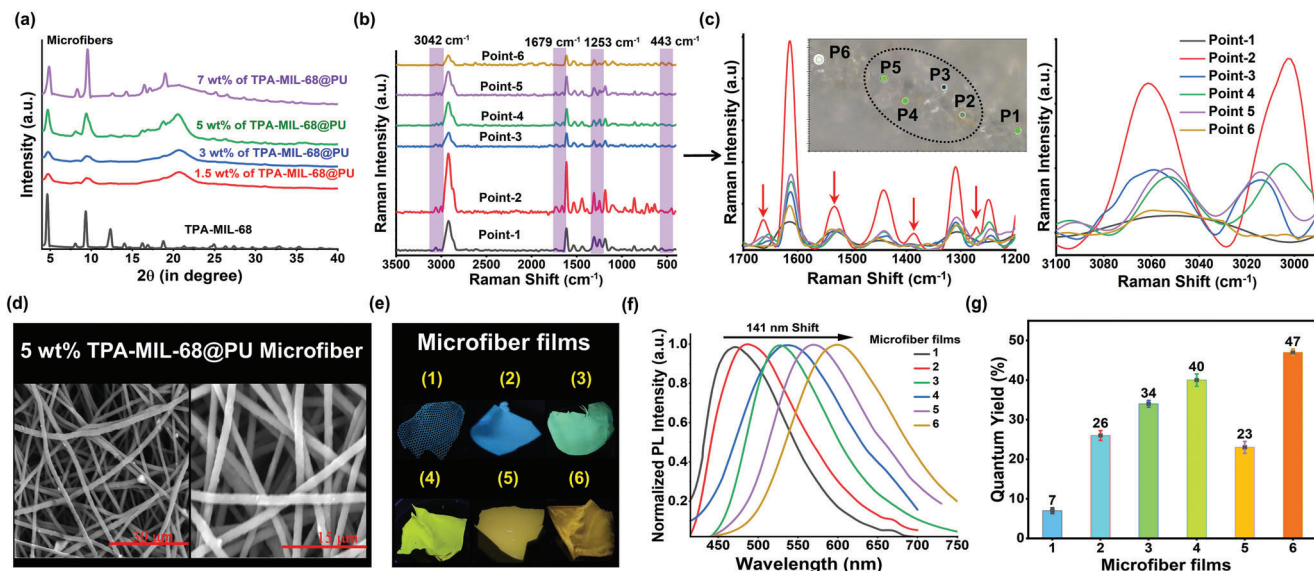


Figure 4. Structural characterization of MOF-fiber composites. a) XPRD patterns of electrospun AIE-MOF fibers demonstrating TPA-MIL-68 presence within the polyurethane (PU) microfibers. b) Micro-Raman spectroscopy was conducted on 5 wt% TPA-MIL-68 fiber, marking six distinct spots of size 2 μm on the fibers to record the local spectra. c) An enlarged image of the different points on the fiber. The inset illustrates the fiber and marked spot; the yellowish spots (P2-P5) denote the AIE-MOF fibers. d) SEM image of 5 wt% TPA-MIL-68 fiber. e–g) Photophysical characterization of electrospun MOF microfibers (1: NH₂-MIL-68-MF, 2: TPE-MIL-68 MF, 3: TPA-MIL-68 MF, 4: TPAth-MIL-68 MF, 5: Py-MIL-68 MF, 6: TPACN-MIL-68 MF). (e) Image of MOF-fiber composites under UV light (365 nm). (f) Photoluminescence emission spectra showing the bathochromic shift. (g) Quantum yield measurements showing the efficiency of the MOF-fiber composites.

supporting the hybridization mechanism further. To resolve disparities in quantum yield, we thoroughly evaluated the lifetimes of each hybridized MOF. The lifetime decay curves in Figure S21 (Supporting Information) show that hybrid AIE-MOFs have a higher decay time than NH₂-MIL-68, indicating that the AIE ligand increases the overall lifetime. The lifetime measurements averaged 5–11 ns (Figure 3f), presenting three distinct components across all hybridized MOFs. Remarkably, in TPACN-MIL-68, the τ_3 component dominates while the τ_1 component recedes, contrasting with other hybrid MOFs (Table S1, Supporting Information). This imbalance implies a more pronounced radiative relaxation process in TPACN-MIL-68, supporting the quantum yield trend we determined.

The photophysical properties of MOFs are greatly influenced by their radiative (K_r) and non-radiative (K_{nr}) decay rates.^[60,61] Specifically, NH₂-MIL-68 and Py-MIL-68, characterized by accelerated non-radiative decay rates, resulted in reduced quantum yields and truncated lifetimes (Figure 3g). In contrast, MOFs, including TPAth-MIL-68 and TPACN-MIL-68, demonstrated a higher value of K_r . Among the hybrid MOFs examined in this study (Figure 3g), TPACN-MIL-68 exhibits the highest radiative efficiency (RE) of $\approx 54\%$. It also displayed the highest quantum yield, which signifies a desirable balance between K_r and K_{nr} , effective MLCT states and increased radiative efficiency. Our findings highlight the potential of ligand engineering in adjusting the photophysical properties of MOFs. Specifically, TPACN-MIL-68 represents a promising area for further research and development. These results also suggest the potential applicability of these MOFs in projects requiring specially engineered electronic properties.

2.3. AIE-MOF Fiber Composites by Electrospinning

Building upon the interest in tunable hybrid MOFs, we have employed electrospinning, a well-established method,^[62] to fabricate thin films. We incorporated MOFs within polyurethane matrices to accomplish this, thereby generating AIE-MOF embedded in polyurethane (AIE-MOF@PU) microfibers. To regulate and standardize the concentration of MOFs within the polyurethane (PU) matrix, we formulated a series of solutions containing varying weight percentages of TPA-MIL-68 concerning the PU solution. These formulated solutions were subsequently subjected to an electrospinning process, facilitating the creation of the desired microfibers. The XPRD pattern in Figure 4a shows the preservation of the AIE-MOF's structural integrity within the fiber matrix. Notably, distinct diffraction peaks, characteristic of the MOF, become discernible when its concentration within the matrix exceeded 3 wt%. This observation underscores the careful balance required to maintain the structural properties of the MOF while integrating it within the PU matrix. To delve into the behavior of the AIE-MOF within the polyurethane matrix, we employed micro-Raman spectroscopy, a non-destructive analytical method based on confocal microscopy. This approach enabled a detailed examination of the interaction between scattered light and the molecular structure of the microfibers, which comprised 7 wt% of the AIE-MOF@PU composite. Micro-Raman spectroscopy furnished a comprehensive representation of the molecular vibrations within the sample, an essential attribute for its precise identification and quantification. Upon conducting micro-Raman analysis on the fiber, we observed pale yellow regions, indicating MOF aggregates (Figure 4c inset). We selected six

distinct spots labelled P-1 through P-6 for further scrutiny for spectral analysis with a spot size of 2 μm .

Interestingly, spots P-1 and P-6 did not present the yellow tint typically associated with the presence of MOF crystals and were initially hypothesized to consist solely of the polymer (Figure 4c). Their corresponding spectra later substantiated this assumption, which lacked the distinct peaks characteristic of AIE-MOF. Conversely, spots P-2 through P-4 exhibited prominent AIE-MOF peaks, such as those at 1675 cm^{-1} , indicative of the imine bond (C = N) (Figure 4b). Additional peaks observed at 1380, 1270 cm^{-1} , 3065, and 3010 cm^{-1} can be attributed to the bending modes of C–H bonds in the aromatic rings, C–N stretching, and C–H stretching modes, respectively (Figure 4c). Notably, in the spectra of P-4 and P-5, a slight shift toward lower energy was observed for the peak at 3055 cm^{-1} , while the peak at 3010 cm^{-1} shifted toward a higher energy. Concurrently, the peak $\approx 1660 \text{ cm}^{-1}$ shifted toward a lower energy compared to the spectra of P-2 and P-3 (Figure 4b,c). These Raman shifts in peak positions suggest alterations in bond behavior within the fiber, possibly attributed to the stretching effect experienced during the electrospinning jet formation process.^[63] The resulting structural confinement restricts the motion of the molecules in fibers. Upon completing the structural characterization, we investigated the fiber's morphology through SEM analysis. We observed a significant correlation between the MOF concentration in the polymer and the resultant fiber morphology. The fibers exhibited a thin profile at concentrations below 5 wt% MOF, with SEM imaging confirming a relatively sparse distribution of MOFs within these fibers (Figures S22a and S22b, Supporting Information). Conversely, at MOF concentrations exceeding 5 wt%, the fibers demonstrated a marked propensity to form beads and aggregates, likely due to an excessive MOF loading in the polymer matrix (Figure S22c, Supporting Information). This uneven distribution and over-saturation of MOFs disrupt the fibers' structural integrity, leading to clumping and bead formation. However, fibers containing 5 wt% of MOFs within the polymer matrix displayed uniformity, devoid of any bead formation (Figure 4d). Our study observed visible aggregates (white powdered), presumably corresponding to the AIE-MOFs, interspersed throughout the fibers. The SEM examination corroborated that a 5 wt% concentration of AIE-MOFs in the polymer was optimal for achieving bead-free and uniform fiber morphology. This observation provides essential insight into the underlying structural dynamics and aids in refining the synthesis process for AIE-MOF@PU microfibers. The SEM observation also complements our Raman spectral analysis, aligning with optimal MOF distribution within the polyurethane matrix. Based on the collective insights from SEM, micro-Raman, and XRD analyses, we incorporated 5 wt% of various hybrid MOFs into the polymer matrix for microfiber preparation. The resulting emissive fibers exhibited a significant bathochromic shift of $\approx 141 \text{ nm}$ compared to the pristine $\text{NH}_2\text{-MIL-68}$ MOF fibers, as shown in Figure 4e,f. The SEM images of all the AIE-MOF@PU fibers showed a complete absence of bead formations (Figure S23, Supporting Information), indicating uniform fiber distribution and confirming the consistency of our synthesis process. Additionally, the calculation of both K_f and K_{nr} processes suggests that the fiber structure enhances radiative decay by imposing constraints on the vibrations of the MOFs within the fiber.

The TPACN@MIL-68 MF fiber exhibited the highest quantum yield of all synthesized fibers (Figure 4g). Interestingly, while TPAth@MIL-68 MF demonstrated a higher K_f , it also has a higher K_{nr} in comparison to TPACN@MIL-68 MF (Table S2, Supporting Information). This elevated K_{nr} influences the overall QY by decreasing the RE% and reducing the proportion of radiative decays, resulting in a lower QY than that observed for TPACN@MIL-68 MF. The highest RE % was observed for TPACN-MIL-68, attributed to its low K_{nr} , which results in a high QY (Figure S24, Supporting Information). The QY of all the AIE-MOF@PU MF were higher than that of powdered AIE-MOFs (Table S3, Supporting Information). The higher QY is due to high RE % than powdered samples. The high RE% of all the microfiber could be attributed to the restriction of the motion of the AIE-MOFs due to the stretching of the fiber during the electrospinning process.^[23,64] Specifically, the electrospinning process forces the molecules to stretch and come into closer proximity with one another, thereby augmenting intermolecular interactions between the molecules. This increased interaction, in turn, restricts the vibrations of the AIE-ligands in AIE-MOFs, leading to an elevation in the radiative constant. This suggests that the fiber formation process might play a crucial role in enhancing the radiative efficiency of the MOFs, underscoring the importance for understanding and optimizing the process parameters in the synthesis of AIE-MOF-based fibers.

2.4. Janus AIE-MOF Fiber Composites by Side-By-Side Electrospinning Method

The advent of white light-emitting Janus fibers signifies a novel and potentially superior approach to conventional methods. This innovation offers enhanced control over light emission characteristics. It facilitates multi functionalities within a singular fiber system, a feat not typically achievable with traditional fibers. The side-by-side electrospinning methods employ a custom designed parallel spinneret to engineer Janus-structured nanofibers. The careful design of the process allows for the precise positioning of specific fluorescent molecules on either side of the nanofibers. This bespoke design allows precise positioning of specific fluorescent molecules on either side of the nanofiber while also allowing the encapsulating polymer matrix to be entirely distinct, creating a fully heterogeneous structure. The distinctive Janus configuration provides spatial separation for different fluorescent AIE hybridized MOFs, a prerequisite for their individual luminescent properties. This method offers notable advantages, including improved quantum yield.

To highlight the versatility of the side-by-side electrospinning method, we carefully engineered an array of solutions integrating TPE-MIL-68 and TPACN-MIL-68 in an 18 wt% PU in a DMF/THF-1:1 solution. By maintaining TPE-MIL-68 at a consistent 5 wt% and judiciously modulating the concentration of TPACN-MIL-68, we successfully fabricated a spectrum of fibers, each exhibiting unique luminescent emission properties. Our analysis revealed that the fibers derived from a 0.5 wt% TPACN-MIL-68 solution emitted green light with corresponding CIE coordinates of (0.32, 0.39). Upon increasing the concentration of TPACN-MIL-68 to 1 wt%, the resulting fibers emitted the desired white light, with CIE coordinates (0.33, 0.34). Intriguingly, when

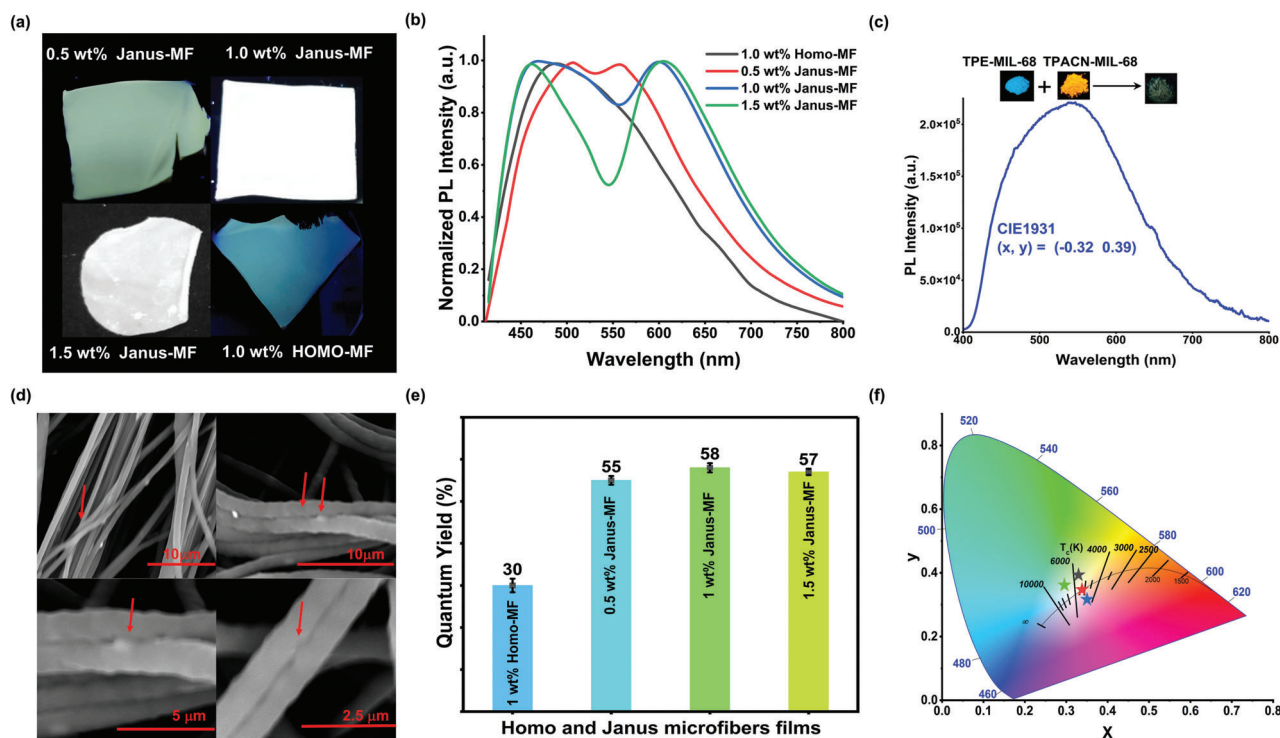


Figure 5. a) Photoluminescence image of Janus fiber with an increasing weight percentage of TPACN-MIL-68 and single-strand homogeneous (“homo”) microfibers. b) Photoluminescent emission spectra of Janus and homo microfibers. c) 1:1 mass ratio mixture of TPE-MIL-68 and TPACN-MIL-68 MOFs. Top: Photos of the mixed AIE-MIL-68 powder under UV light (365 nm), exhibiting a greenish-blue emission. Bottom: Emission spectra of the mixed AIE-MOF powder under UV excitation. The CIE1931 coordinates are (0.35, 0.39), corresponding to a greenish-blue emission. d) SEM images, e) quantum yield and f) CIE coordinates of Janus and homo microfibers.

we further escalated the concentration to 1.5 wt%, the fibers exhibited a distinct whitish-pink emission, traced back to CIE coordinates of (0.36, 0.31). (Figure 5a,b,f)

A control experiment was conducted to extend our understanding. We first fabricated the homogeneous microfiber (HOMO-MF) by mixing the 5 wt% TPE-MIL-68 solution with the 1 wt% TPACN-MIL-68 solution. The resulting microfiber emitted bluish-green light, corroborated by CIE coordinates of (0.29, 0.36) (Figure 5f). We also attempted mechanical mixing, where the two powders (TPE-MIL-68 and TPACN-MIL) were mixed in a 1:1 mass ratio. However, physical mixing did not yield white light (Figure 5c).

The SEM image of the 1 wt% Janus microfiber (Janus-MF) unequivocally exhibited the Janus structure, complete with clearly delineated boundaries for both fibers, manifesting the efficacy of the side-by-side electrospinning technique (Figure 5d). The SEM images of the fibers derived from 0.5 and 1.5 wt% TPACN-MIL-68 solutions provided additional insights; they depicted coalescence of fibers side by side where bunches of fibers adhered to one another (Figures S25a & S25b, Supporting Information). In contrast, the SEM micrographs of the HOMO-MF (Figure S25c, Supporting Information) showed a higher degree of MOF aggregation compared with the Janus MF.

The emitted white light from these Janus microfibers falls within the “Daylight” category, exhibiting color temperatures between 5000–6000 K (Figure 5f). Such characteristic, reminiscent of the balanced and vibrant light of the midday sun, is highly

sought after in practical applications.^[20] When coupled with their QY, these fibers underscore the advantage of the Janus microfibers synthesized from hybrid TPACN-MIL-68 solutions at concentrations of 0.5, 1, and 1.5 wt%, exhibiting QY values of 55, 58, and 57%, respectively (Figure 5e). These values represent a significant improvement over the 30% QY of the HOMO-MF. Upon consideration of the related literature available (see Table S4 in the Supporting Information), these results are comparable to the highest quantum efficiencies observed for hybrid AIE-MOFs,^[19,20,65] specifically for white light emissive materials based on AIE-MOF- Janus fiber composite.

A deeper analysis of the lifetime data for the fibers reveals that, compared to the HOMO-MF, the Janus microfiber exhibited a pronounced τ_3 component at longer wavelengths (Figure S26, Supporting Information). Moreover, as the weight percentage of the TPACN-MIL-68 increased, the contribution from the τ_1 component diminished. This trend suggests that the presence of TPACN-MIL-68 promotes a shift toward the radiative transition state. The fluorescence lifetime decay of the 1 wt% Janus MF was scrutinized at different emission wavelengths (Figure 6). At higher wavelengths, it can be seen that where strong blue emission occurred, the contributions from the τ_1 and τ_2 components were substantial.

However, as the emission wavelength decreased, the τ_2 component’s contribution declined, while the τ_3 component’s contribution escalated (Figure 6), which confirm the incorporation of AIE-MOF powders within the Janus fibers. Upon calculat-

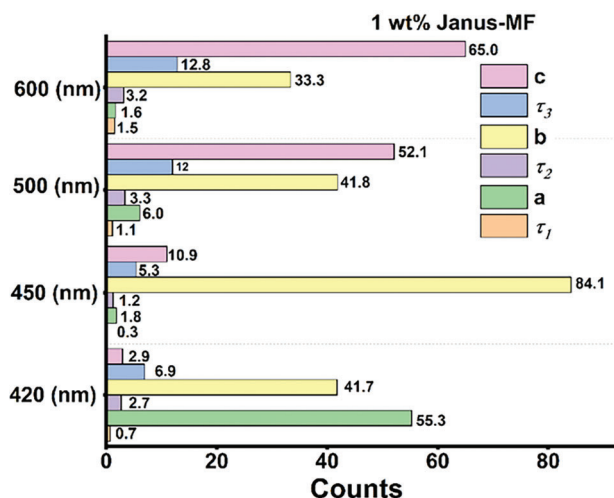


Figure 6. Showing the excited state lifetime with components (τ_1 , τ_2 , and τ_3) in ns, including the relative amplitude (a , b , and c) percentage at different emission wavelengths of 1 wt% of Janus microfiber.

ing the radiative and non-radiative decay rates, it was evident that the radiative efficiency increased in the Janus type of fiber compared to the Homo-MF (Figure S27, Supporting Information). The high efficiency of Janus nanofiber was due to the increase of the charge transfer state efficiency and without any energy transfer effect between the donor and acceptor.^[35,65,66] Typically in Janus-type materials, the substantial spatial separation between emitters situated in different fiber strands renders energy transfer improbable. A scrutiny of the lifetime decay profiles (Figure S28, Supporting Information) reveals an extended lifetime for Janus microfibers compared to HOMO microfibers, indicating that energy transfer between TPE and TPACN is hindered. This suggests that the Janus-MFs are more efficient at converting absorbed light into emitted light. This observation underscores the distinct photophysical behavior of the Janus microfibers compared to the HOMO-MF and loose powders of AIE-MOFs.

3. Conclusion

This work initially focused on synthesizing and engineering a diverse range of D-A type AIE-active ligands. With careful manipulation and design, we successfully adjusted the emission properties of the hybrid AIE-MOFs, as confirmed and detailed by nanoFTIR and XPS characterization. This initial step validated the hybridization process and offered a comprehensive understanding of the tunable emission across the visible spectrum. Subsequently, we incorporated these hybrid AIE-MOFs into PU polymers, transforming them into flexible electrospun microfibers. By doing so, we could fine-tune the fiber's emission properties, significantly enhancing the photoluminescent quantum efficiency.

Further studies on the interactions between AIE-MOF and fibers using micro-Raman spectroscopy concluded that the molecular interaction increases the restriction of molecular motion, thereby increasing the radiative efficiency of the fiber, resulting in enhanced QY. The study also highlights the fabrication

of Janus-type white light-emitting hybrid AIE-MOF fiber composites. Utilizing the side-by-side electrospinning technique, we optimized our solutions, leading to the precise positioning of specific fluorescence AIE hybridized MOFs on either side of the nanofiber. The distinctive Janus structure, as evidenced by SEM images, is a testament to the effectiveness of our approach. Furthermore, we interrogated the photophysical properties of the AIE-MOFs, by contrasting the photophysical performance between powdered samples and fibers. This comparison accentuated that the AIE-hybrid MOFs fibers exhibit a superior quantum yield compared to the AIE-MOFs. Remarkably, we also achieved a high quantum yield of 58% for the Janus fibers, showcasing a substantial enhancement in performance. Systematic analysis of lifetime decay, radiative efficiency, and non-radiative efficiency rendered a holistic understanding of the mechanisms underpinning the significantly improved performance of these AIE-active MOF-based fibers.

In conclusion, this research presents a step change in the approach for developing high-performance white light-emitting materials, from the initial ligand engineering to the final fabrication of Janus fibers. The results highlight the potential of hybrid AIE-MOFs in advancing optoelectronic applications, marked by a significant increase in the quantum yield, tunable emission properties and improved understanding of the underlying photophysics.

4. Experimental Section

Synthesis of AIE ligands and MOFs, structure elucidation, additional spectroscopic details and computational details can be found in the Supporting Information.

Electronic structure calculations were carried out using Gaussian 09 program suite^[67] with the hybrid functional B3LYP (the Becke three-parameter exchange functional,^[68] and Lee-Yang-Parr correlation functional^[69]), and all the electrons with the 6311 G(d,p) basis set.

Supporting Information

Supporting Information is available from the Wiley Online Library or from the author.

Acknowledgements

V.K., S.M., and J.C.T. thank the ERC Consolidator Grant PROMOFS (grant agreement 771575) and ERC Proof-of-Concept Grant LUMIVOCS (grant agreement 957504) for funding the research. J.C.T. acknowledges the EP-SRC IAA award (EP/R511742/1) for additional support. The author thank the Research Complex at Harwell (RCaH) for providing materials characterization facilities and Dr Shaoliang Guan for XPS analysis.

Conflict of Interest

The authors declare no conflict of interest.

Data Availability Statement

The data that support the findings of this study are available from the corresponding author upon reasonable request.

Keywords

AIE-MOFs, high quantum yield, Janus fiber, luminescent fiber composites, tunable emission, white light emission

Received: July 13, 2023
Revised: October 8, 2023
Published online: October 27, 2023

- [1] X. Zheng, W. Zhu, C. Zhang, Y. Zhang, C. Zhong, H. Li, G. Xie, X. Wang, C. Yang, *J. Am. Chem. Soc.* **2019**, *141*, 4704.
- [2] S. Wu, D. Ren, K. Zhou, H.-L. Xia, X.-Y. Liu, X. Wang, J. Li, *J. Am. Chem. Soc.* **2021**, *143*, 10547.
- [3] D. Ren, H.-L. Xia, K. Zhou, S. Wu, X.-Y. Liu, X. Wang, J. Li, *Angew. Chem., Int. Ed.* **2021**, *60*, 25048.
- [4] M. Gutiérrez, Y. Zhang, J.-C. Tan, *Chem. Rev.* **2022**, *122*, 10438.
- [5] L. Sun, W. Zhu, X. Zhang, L. Li, H. Dong, W. Hu, *J. Am. Chem. Soc.* **2021**, *143*, 19243.
- [6] X.-Y. Liu, W. P. Lustig, J. Li, *ACS Energy Lett.* **2020**, *5*, 2671.
- [7] H.-L. Xia, K. Zhou, S. Wu, D. Ren, K. Xing, J. Guo, X. Wang, X.-Y. Liu, J. Li, *Chem. Sci.* **2022**, *13*, 8036.
- [8] Z. Li, F. Jiang, M. Yu, S. Li, L. Chen, M. Hong, *Nat. Commun.* **2022**, *13*, 2142.
- [9] Y. Zhang, T. Xiong, A. F. Mölslein, S. Mollick, V. Kachwal, A. S. Babal, N. Amin, J.-C. Tan, *Appl. Mater. Today* **2022**, *27*, 101434.
- [10] Y. Huang, W. Feng, Z. Zhou, H. Zheng, Y. Zhao, H. Yan, X. Lü, *J. Mater. Chem. C* **2022**, *10*, 7586.
- [11] H.-Q. Yin, X.-Y. Wang, X.-B. Yin, *J. Am. Chem. Soc.* **2019**, *141*, 15166.
- [12] X. Zhai, Z. Cui, W. Shen, *Inorg. Chem. Commun.* **2022**, *146*, 110038.
- [13] J. Dong, P. Shen, S. Ying, Z.-J. Li, Y. D. Yuan, Y. Wang, X. Zheng, S. B. Peh, H. Yuan, G. Liu, Y. Cheng, Y. Pan, L. Shi, J. Zhang, D. Yuan, B. Liu, Z. Zhao, B. Z. Tang, D. Zhao, *Chem. Mater.* **2020**, *32*, 6706.
- [14] Y. Liu, X. Guan, Q. Fang, *Aggregate* **2021**, *2*, e34.
- [15] Z.-H. Zhu, C. Bi, H.-H. Zou, G. Feng, S. Xu, B. Z. Tang, *Adv. Sci.* **2022**, *9*, 2200850.
- [16] X. Shi, X. Yan, H.-B. Yang, in *Handbook of Aggregation-Induced Emission*, John Wiley & Sons Ltd, Chichester, West Sussex, UK **2022**, 367, ch. 14.
- [17] K. T. Smith, K. Hunter, N.-C. Chiu, H. Zhuang, P. Jumrusprasert, W. F. Stickle, J. A. Reimer, T. J. Zuehlsdorff, K. C. Stylianou, *Angew. Chem., Int. Ed.* **2023**, *62*, e202302123.
- [18] Y. Y. Liu, X. Zhang, K. Li, Q. C. Peng, Y. J. Qin, H. W. Hou, S. Q. Zang, B. Z. Tang, *Angew. Chem., Int. Ed.* **2021**, *60*, 22417.
- [19] Y. Yang, W. Li, C. Sun, G. Shan, C. Qin, K. Shao, J. Wang, Z. Su, *Adv. Opt. Mater.* **2022**, *10*, 2200174.
- [20] N.-C. Chiu, K. T. Smith, K. C. Stylianou, *Coord. Chem. Rev.* **2022**, *459*, 214441.
- [21] W. Ji, X. Wang, T. Ding, S. Chakir, Y. Xu, X. Huang, H. Wang, *Chem. Eng. J.* **2023**, *451*, 138973.
- [22] L. Zhang, G. M. Biesold, C. Zhao, H. Xu, Z. Lin, *Adv. Mater.* **2022**, *34*, 2200776.
- [23] V. Kachwal, J.-C. Tan, *Adv. Sci.* **2023**, *10*, 2204848.
- [24] H.-J. Yen, J.-H. Wu, W.-C. Wang, G.-S. Liou, *Adv. Opt. Mater.* **2013**, *1*, 668.
- [25] R. Dong, Y. Li, M. Chen, P. Xiao, Y. Wu, K. Zhou, Z. Zhao, B. Z. Tang, *Small Methods* **2022**, *6*, 2101247.
- [26] Y. Zhang, J.-C. Tan, *iScience* **2021**, *24*, 103035.
- [27] K. Y. Kim, S. H. Jung, J. H. Jung, *J. Mater. Chem. B* **2015**, *3*, 7222.
- [28] W. Yu, X. Yu, Z. Qiu, C. Xu, M. Gao, J. Zheng, J. Zhang, G. Wang, Y. Cheng, M. Zhu, *Chem. - Eur. J.* **2022**, *28*, e202201664.
- [29] C. Ma, Z. Li, C. Zhang, G. Xie, Y. Wu, Y. Zhang, J. Mo, X. Liu, K. Wang, D. Xie, Y. Li, *Front. Chem.* **2021**, *9*, 727631.
- [30] D.-G. Yu, J.-J. Li, M. Zhang, G. R. Williams, *Chem. Commun.* **2017**, *53*, 4542.
- [31] Z. Lamberger, S. Zainuddin, T. Scheibel, G. Lang, *ChemPlusChem* **2023**, *88*, 202200371.
- [32] Z. Peng, J. Huang, Z. Guo, *Nanoscale* **2021**, *13*, 18839.
- [33] Z. Qin, X. Chen, Y. Yin, G. Ma, Y. Jia, J. Deng, K. Pan, *Adv. Mater. Technol.* **2020**, *5*, 1900859.
- [34] H. Zhang, L. Sun, J. Guo, Y. Zhao, *Research* **2023**, *6*, 0129.
- [35] S. Zhao, J. Sun, Z. Qin, Y. Li, H. Yu, G. Wang, X. Gu, K. Pan, *Small* **2022**, *18*, 2201117.
- [36] S. Farhaj, B. R. Conway, M. U. Ghorri, *Fibers* **2023**, *11*, 21.
- [37] T. Zhang, Q. Cheng, J. H. Lei, B. Wang, Y. Chang, Y. Liu, G. Xing, C. Deng, Z. Tang, S. Qu, *Adv. Mater.* **2023**, *35*, 2302705.
- [38] S. Mollick, S. Saurabh, Y. D. More, S. Fajal, M. M. Shirolkar, W. Mandal, S. K. Ghosh, *Energy Environ. Sci.* **2022**, *15*, 3462.
- [39] Y. Yang, J. Cheng, B. Wang, Y. Guo, X. Dong, J. Zhao, *Microchim. Acta* **2019**, *186*, 101.
- [40] A. Kertik, L. H. Wee, K. Sentosun, J. A. R. Navarro, S. Bals, J. A. Martens, I. F. J. Vankelecom, *ACS Appl. Mater. Interfaces* **2020**, *12*, 2952.
- [41] B. Hosseini Monjezi, B. Sapotta, S. Moulai, J. Zhang, R. Oestreich, B. P. Ladewig, K. Müller-Buschbaum, C. Janiak, T. Hashem, A. Knebel, *Chem. Ing. Tech.* **2022**, *94*, 135.
- [42] Z. Sharifzadeh, A. Morsali, *Coord. Chem. Rev.* **2022**, *459*, 214445.
- [43] R. Liang, R. Huang, X. Wang, S. Ying, G. Yan, L. Wu, *Appl. Surf. Sci.* **2019**, *464*, 396.
- [44] D. Li, T. Hua, X. Li, J. Cheng, K. Du, Y. Hu, Y. Chen, *Chemosphere* **2022**, *292*, 133461.
- [45] Y. Pi, X. Li, Q. Xia, J. Wu, Z. Li, Y. Li, J. Xiao, *Nano Res.* **2017**, *10*, 3543.
- [46] A. F. Mölslein, L. Donà, B. Civalieri, J.-C. Tan, *ACS Appl. Nano Mater.* **2022**, *5*, 6398.
- [47] Y. Cai, P. Liang, Q. Tang, X. Yang, W. Si, W. Huang, Q. Zhang, X. Dong, *ACS Nano* **2017**, *11*, 1054.
- [48] K. H. Horn, N. Lehnert, F. Tuczek, *Inorg. Chem.* **2003**, *42*, 1076.
- [49] L. Shen, S. Liang, W. Wu, R. Liang, L. Wu, *Dalton Trans.* **2013**, *42*, 13649.
- [50] P. Manna, B. K. Tripuramallu, S. K. Das, *Cryst. Growth Des.* **2014**, *14*, 278.
- [51] Z. Wei, Z.-Y. Gu, R. K. Arvapally, Y.-P. Chen, R. N. Mcdougald, J. F. Ivy, A. A. Yakovenko, D. Feng, M. A. Omary, H.-C. Zhou, *J. Am. Chem. Soc.* **2014**, *136*, 8269.
- [52] J. R. Lakowicz, J. Malicka, S. D'auria, I. Gryczynski, *Anal. Biochem.* **2003**, *320*, 13.
- [53] K. Röttger, N. K. Schwalb, F. Temps, *J. Phys. Chem. A* **2013**, *117*, 2469.
- [54] F. Zhang, X. Liu, F. Huang, Z. Zhuo, L. Lu, Z. Xu, Y. Wang, X. Tao, W. Bian, W. Tang, *Chin. Sci. Bull.* **2011**, *56*, 479.
- [55] Z. Wang, J.-J. Liu, S.-Y. Yin, M.-Y. Li, Y.-J. Hou, D. Wang, J.-T. Mo, G. Chen, *Adv. Funct. Mater.* **2023**, *33*, 2212985.
- [56] C. A. Kent, D. Liu, L. Ma, J. M. Papanikolas, T. J. Meyer, W. Lin, *J. Am. Chem. Soc.* **2011**, *133*, 12940.
- [57] R. Haldar, A. Ghosh, T. K. Maji, *Chem. Commun.* **2023**, *59*, 1569.
- [58] J. Zhang, G. Frenking, *J. Phys. Chem. A* **2004**, *108*, 10296.
- [59] T. Huyen Vu, N. Serradji, M. Seydou, É. Brémond, N.-T. Ha-Duong, *J. Inorg. Biochem.* **2020**, *203*, 110864.
- [60] S. Mollick, T. N. Mandal, A. Jana, S. Fajal, S. K. Ghosh, *Chem. Sci.* **2019**, *10*, 10524.
- [61] W. P. Lustig, S. J. Teat, J. Li, *J. Mater. Chem. C* **2019**, *7*, 14739.
- [62] S. Cavaliere, S. Subianto, I. Savych, D. J. Jones, J. Rozière, *Energy Environ. Sci.* **2011**, *4*, 4761.
- [63] D. H. Reneker, A. L. Yarin, *Polymer* **2008**, *49*, 2387.
- [64] H. Li, H. Wen, Z. Zhang, N. Song, R. T. K. Kwok, J. W. Y. Lam, L. Wang, D. Wang, B. Z. Tang, *Angew. Chem., Int. Ed.* **2020**, *59*, 20371.
- [65] A. Karmakar, J. Li, *Chem. Commun.* **2022**, *58*, 10768.
- [66] Z. Qin, Q. Wang, C. Wang, D. Xu, G. Ma, K. Pan, *J. Mater. Chem. C* **2019**, *7*, 1065.
- [67] M. Frisch, G. Trucks, H. B. Schlegel, G. Scuseria, M. Robb, J. Cheeseman, G. Scalmani, V. Barone, G. Petersson, H. Nakatsuji, Gaussian Inc., Wallingford CT **2016**.
- [68] A. D. Becke, *Phys. Rev. A* **1988**, *38*, 3098.
- [69] A. D. Becke, *J. Chem. Phys.* **1993**, *98*, 5648.